Electronic Supplementary Material (ESI) for Nanoscale.

Supplementary Material Section

Visualisation of central-cell-effects in simulated scanning-tunnelling-microscope images of subsurface dopant qubits in silicon

M. Usman[1], B. Voisin[2], J. Salfi[2], S. Rogge[2], and L.C.L. Hollenberg[1]
[1] *Center for Quantum Computation and Communication Technology, The School of Physics, The University of Melbourne, Parkville, 3010, Victoria Australia*
[2] *Centre for Quantum Computation and Communication Technology, School of Physics, The University of New South Wales, Sydney, 2052, NSW, Australia.*

S1. Atomistic Modelling of Donor Wave Functions

The atomistic simulations of electronic energies and states for a dopant in silicon are performed by solving an $sp^3d^5s^*$ tight-binding Hamiltonian. The $sp^3d^5s^*$ tight-binding parameters for the Si material are obtained from Boykin *et al.* [1], which have been optimised to accurately reproduce the Si bulk band structure. The phosphorous dopant atom is represented by a central-cell-correction (CCC) model. For this study, we have implemented two central-cell-correction models, namely $\mathrm{CCC^S}$ and $\mathrm{CCC^{NS}}$. In the $\mathrm{CCC^S}$ model, a Coulomb-like donor potential is screened by static dielectric constant ($\epsilon(0)$) of silicon material and is given by:

$$U\left(r\right)=\frac{-e^2}{\epsilon\left(0\right)r} \tag{1}$$

where $\epsilon(0)=11.9$ is the static dielectric constant of Si and e is the charge on electron. The potential is cut-off to $\mathrm{U}(r_0)=\mathrm{U}_0$ at the donor site, where the value of U_0 is adjusted to match the experimentally measured binding energy spectra of 1s states [2].

The second CCC model is much more extensive as it includes intrinsic strain and non-static dielectric screening effects [3]. The donor atom is again represented by a Coulomb-like potential, which is cut-off to $\mathrm{U}(r_0)=\mathrm{U}_0$ at the donor site, however it is screened by a k-dependent dielectric function and is given by:

$$U\left(r\right)=\frac{-e^2}{\epsilon\left(0\right)r}\left(1+A\epsilon\left(0\right)\mathrm{e}^{-\alpha r}+\left(1-A\right)\epsilon\left(0\right)\mathrm{e}^{-\beta r}-\mathrm{e}^{-\gamma r}\right) \tag{2}$$

where A, α, β, and γ are fitting constant and have been numerically fitted as described in the literature [4]. Additionally, the nearest-neighbor bond-lengths of Si:P are strained by 1.9% in accordance with the recent DFT study [5].

The size of the simulation domain (Si box around the dopant) is chosen as 40 nm^3, consisting of roughly 3 million atoms, with closed boundary conditions in all three spatial dimensions. The effect of Hydrogen passivation on the surface atoms is implemented in accordance with our published recipe [6], which shifts the energies of the dangling bonds to avoid any spurious states in the energy range of interest. The multi-million-atom real-space Hamiltonian is solved by a parallel Lanczos algorithm to calculate the single-particle energies and wave functions of the dopant atom. The tight-binding Hamiltonian is implemented within the framework of NEMO-3D [7, 8].

In the reported STM experiments [9], the (001) sample surface consists of dimer rows of Si atoms. We have incorporated this effect in our atomistic theory by implementing 2×1 surface reconstruction scheme, in which the surface silicon atoms are displaced in accordance with the published studies [10]. The impact of the surface strain due to the 2×1 reconstruction is included in the tight-binding Hamiltonian by a

generalization of the Harrison's scaling law [1], where the inter-atomic interaction energies are modified with the strained bond length d as $(\frac{d_0}{d})^\eta$, where d_0 is the unperturbed bond-length of Si lattice and η is a scaling parameter whose magnitude depends on the type of the interaction being considered and is fitted to obtain hydrostatic deformation potentials.

The contact hyperfine interaction (A) is directly proportional to the charge density of the ground state wave function at the donor site $|\Psi_{\mathrm{D}}|^2$, and the excited states do not contribute in the magnitude of A [11]. The Z-valley population of the donor ground states is calculated by following the procedure described in the supplementary information of Salfi et al. [9]. The size of the spatial distribution of the donor wave functions is defined in terms of its mean radius of in-plane (1/100)-contours – a contour where the amplitude of the normalised wave function decreases to 1/100 value. A direct comparison of these parameters computed from the two CCC models is presented in figure S1.

One important parameter of interest for exchange-based two qubit quantum logic gate design is the strength of exchange interaction (J) between two P donor atoms. Previous theoretical calculations have shown that the calculation of exchange interaction is very sensitive to the implementation of central-cell corrections [12–14]. We have computed the exchange interaction energies (J) for the two CCC models by using the Heitler-London formalism [15] as shown in figure S1 (d), and our calculations indicate a clear dependence of J on the implementation of CCC.

S2. Computation of STM Images

The calculation of the STM images is implemented by coupling the Bardeen's tunnelling theory [16] and Chen's derivative rule [17] with our tight-binding wave function. In the tunnelling regime, the relationship between the applied bias (V) on the STM tip and the tunnelling current (I) is provided by the Bardeen's formula:

$$I_T(V) = \frac{2\pi e}{\hbar}\sum_{\mu\nu}(1 - f(E_\nu + eV))|M_{\mathrm{DT}}|^2 \times \delta(E_\mu - E_\nu - eV) \tag{3}$$

where e is the electronic charge, $\hbar$ is the reduced Planck's constant, f is the Fermi distribution function, and M_{DT} is the tunnelling matrix element between the single electron states of the dopant (denoted by the subscript D) and of the STM tip (denoted by the subscript T). As derived by Chen in Ref. 17 that the tunnelling matrix element, for all the cases related to STM measurements, can be reduced to a much simpler surface integral solved on a separation surface χ arbitrarily chosen at a point in-between the sample and STM tip. Therefore,

$$M_{\mathrm{DT}} = \frac{\hbar^2}{2m_e}\int_\chi (\Psi^*_{\mathrm{T}}\nabla\Psi_{\mathrm{D}} - \Psi_{\mathrm{D}}\nabla\Psi^*_{\mathrm{T}}).d\chi \tag{4}$$

where Ψ_{D} is the single electron state of the sample (P or As dopant in Si), Ψ_{T} is the state of the single atom at the apex of the STM tip, and $d\chi$ is an element on the separation surface χ.

In our calculation of the STM images, we follow Chen's approach [17], which reduces equation 4 to a very simple derivative rule where the tunnelling matrix element is simply proportional to a functional of the sample wave function computed at the tip location, r_0 (for χ assumed to be at the apex of the STM tip):

$$M_{\mathrm{DT}} \propto \Im[\Psi_{\mathrm{D}}(r)] \tag{5}$$

where the functional of the wave function, $\Im[\Psi_{\mathrm{D}}(r)]$, is defined as a derivative (or the sum of derivatives) of the sample wave function – the direction and the dimensions of the derivatives depend on the orbital composition of the STM tip state. In our recent study [18], we have shown that the tip orbital that

dominates the STM tunnelling current is $d_{z^2-\frac{1}{3}r^2}$ orbital, for which the equation 5 becomes:

$$M_{\mathrm{DT}} \propto \frac{2}{3}\frac{\partial^2\Psi_{\mathrm{D}}(r)}{\partial z^2} - \frac{1}{3}\frac{\partial^2\Psi_{\mathrm{D}}(r)}{\partial y^2} - \frac{1}{3}\frac{\partial^2\Psi_{\mathrm{D}}(r)}{\partial x^2} \tag{6}$$

The calculation of tunneling current is based on evaluating equation 6 at the the tip position. For this, we calculate the derivatives of the dopant wave function $\Psi_{\mathrm{D}}(r)$ at the tip location, by computing its vacuum decay based on the Slater orbital real-space dependence [22], which satisfies the vacuum Schrödinger equation. Since the derivation of tight-binding Hamiltonian is independent of exact form of basis orbitals, the choice of basis orbitals is arbitrary. However the previous studies [23, 24] have shown that the use of Slater-type orbitals works well in the tight-binding theory as they accurately capture the atomic-scale screening of the materials. The analytical form of Slater-type orbitals for silicon material is given in Ref. [24], which has been used in this work to describe real-space representation of the donor wave function.

It should be noted that the applied bias on STM tip was chosen to induce a small electric field, of the order of -0.3 ± 1.9 MV/m [9]. The electric fields of such magnitudes are expected to negligibly perturb the real-space distribution and valley-population of the ground state of subsurface donors. Furthermore, when the STM tip bias was adjusted to introduce much larger electric field of the magnitude 10 MV/m, the valley population of the donor state was changed by less than 1% [25]. Therefore in this work, we ignore the effect of electric field induced by the STM tip bias.

Finally, our low temperature STM data precludes the Si-tip model used to explain force-distance spectroscopies. This is not surprising because we work on chemically inert hydrogen terminated surfaces, at low temperature 4.2 K where chemical reactions will be highly suppressed.

S3. Fourier Domain Analysis of STM Images

Figure S3 plots the Fourier transform of the real-space images of P donor in $\mathrm{L}^5_{1/2}(0)$, $\mathrm{L}^5_{1/5}(1)$, and $\mathrm{L}^5_{1/2}(2)$ locations, computed from both $\mathrm{CCC}^{\mathrm{S}}$ and $\mathrm{CCC}^{\mathrm{NS}}$ models. Since the real-space images computed from $\mathrm{CCC}^{\mathrm{NS}}$ model exhibit larger spatial extent (see Figure 2 in the main text), so the Fourier domain image exhibit lower amplitude in the frequency profile.

The ground state of a bulk P donor is comprised of equal contributions form six k-space degenerate valleys. When the donor atom is brought closer to the Z=0 surface, it increases the Z-valley population and correspondingly X and Y valley populations decrease. The STM images directly probe the donor wave functions, therefore in the Fourier spectrum of the STM images, the k-space valley information should be visible. As it turned out, that due to the strong inter-valley interference arising from the cross terms in $|\Psi_{\mathrm{D}}(k)|^2$ and second derivatives involved due to dominant tunnelling from $d_{z^2-\frac{1}{3}r^2}$ tip orbital, the components of the Fourier transform of STM images only provide information about the interference of X, Y, and Z valleys. From the previously published analysis [9], it has been shown that the frequency amplitudes in the so-called side-lobe ratios are qualitatively related to the corresponding X=Y valley populations of the donor wave functions. Figure S3 (b) plots the Z-valley populations directly extracted from the Fourier spectrum of the donor wave functions, as function of the donor depths, computed from both $\mathrm{CCC}^{\mathrm{S}}$ and $\mathrm{CCC}^{\mathrm{NS}}$ models. For both models, the Z-valley population increases as the donor atom becomes closer to the (001) surface. The larger increase in the Z-valley population for the $\mathrm{CCC}^{\mathrm{NS}}$ model is due to larger spatial extent of the corresponding wave function closer to the donor atom, which strongly interact with the interface as the donor atom is very close to the surface. To correlate this effect with the STM images, we also plot the k_x=k_y cut for $\mathrm{L}^5_{1/2}(2)$ in figure S3 (c). The amplitude of the frequencies in the side-lobes is weaker for the $\mathrm{CCC}^{\mathrm{NS}}$ model compared to the $\mathrm{CCC}^{\mathrm{S}}$ model, which indicates low (high) population for XY (Z) valleys, consistent with the results of figure S3 (b). As the valley physics is a fundamental parameter of the donor wave functions directly modulated by the underlying CCC implementations, its direct availability in the Fourier spectrum of the STM images provides a viable path towards fine tuning of the CCC parameters directly based on STM measurements.

S4. Comparison of As and P STM Images

The ground state binding energies of the P and As donors are 45.5 meV and 53.7 meV as measured by the experiment [26], therefore the As wave function is much more tightly bounded to the donor atom compared to the P wave function. This is captured in the central-cell-effects by having a larger value of the cut-off potential U_0 for the As donor, which is 1.3 eV higher than for the P atom [11]. As a result, the STM images for As donor are expected to be have small spatial size (and larger frequency components). Figure S4 compares the real space and Fourier space images of the As and P donors in panels (a) and (b), respectively. The donors are placed at the same atomic sites in $L^7_{3/4}(0)$, $L^7_{3/4}(1)$, and $L^7_{3/4}(2)$. The difference between the STM images of As and P donors are quite evident, which indicates that STM imaging technique could differentiate between As and P donors. In fact, in future, if an experiment is performed by placing P and As atoms at the same lattice location, a direct comparison between the two measurements could provide a way to fine tune central-cell effects.

[1] T. B. Boykin, G. Klimeck, and F. Oyafuso, Phys. Rev. B **69**, 115201 (2004).
[2] S. Ahmed, N. Kharche, R. Rahman, M. Usman, S. Lee, H. Ryu, H. Bae, S. Clark, B. Haley, M. Naumov, F. Saied, M. Korkusinski, R. Kennel, M. McLennan, T. B. Boykin, and G. Klimeck, "Multimillion atom simulations with nemo3d," in *Encyclopedia of Complexity and Systems Science*, edited by R. A. Meyers (Springer New York, New York, NY, 2009) pp. 5745–5783.
[3] M. Usman, R. Rahman, J. Salfi, J. Bocquel, B. Voisin, S. Rogge, G. Klimeck, and L. C. L. Hollenberg, J. Phys.: Cond. Matt. **27**, 154207 (2015).
[4] H. Nara, J. Phys. Soc. Jap. **20**, 778 (1965).
[5] H. Overhof and U. Gerstmann, Phys. Rev. Lett. **92**, 087602 (2004).
[6] S. Lee *et al.*, Phys. Rev. B **69**, 045316 (2004).
[7] G. Klimeck, S. Ahmed, H. Bae, N. Kharche, S. Clark, B. Haley, S. Lee, M. Naumov, H. Ryu, F. Saied, M. .Prada, M. Korkusinski, T. B. Boykin, and R. Rahman, IEEE Trans. Elect. Dev. **54**, 2079 (2007).
[8] G. Klimeck, S. Ahmed, N. Kharche, M. Korkusinski, M. Usman, M. Parada, and T. Boykin, IEEE Trans. Elect. Dev. **54**, 2090 (2007).
[9] J. Salfi, J. A. Mol, R. Rahman, G. Klimeck, M. Y. Simmons, L. C. L. Hollenberg, and S. Rogge, Nature Materials **13**, 605 (2014).
[10] B. I. Craig and P. V. Smith, Surface Science **226**, L55 (1990).
[11] M. Usman, C. D. Hill, R. Rahman, G. Klimeck, M. Y. Simmons, S. Rogge, and L. C. L. Hollenberg, Phys. Rev. B **91**, 245209 (2015).
[12] C. J. Wellard and L. C. L. Hollenberg, Phys. Rev. B **72**, 085202 (2005).
[13] G. Pica *et al.*, Phys. Rev. B **89**, 235306 (2014).
[14] A. L. Saraiva *et al.*, J. Phys.: Condens. Matter **27**, 154208 (2015).
[15] C. Wellard *et al.*, Phys. Rev. B **68**, 195209 (2003).
[16] J. Bardeen, Phys. Rev. Lett. **6**, 57 (1961).
[17] C. J. Chen, Phys. Rev. B **42**, 8841 (1990-I).
[18] M. Usman, J. Bocquel, J. Salfi, B. Voisin, A. Tankasala, R. Rahman, M. Y. Simmons, S. Rogge, and L. Hollenberg, Nature Nanotechnology **11**, 763 (2016).
[19] J. M. Blanco *et al.*, Prog. Surf. Sci. **81**, 403 (2006).
[20] A. N. Chaika, S. S. Nazin, V. N. Semenov, S. I. Bozhko, O. Lubben, S. A. Krasnikov, K. Radican, and I. V. Shvets, Euro Phys. Lett. **92**, 46003 (2010).
[21] G. Teobaldi, E. Inami, J. Kanasaki, K. Tanimura, and A. L. Shluger, Phys. Rev. B **85**, 085433 (2012).
[22] J. C. Slater, Phys. Rev. **36**, 57 (1930).
[23] S. Lee *et al.*, Phys. Rev. B **63**, 195318 (2001).
[24] E. Nielsen, R. Rahman, and R. P. Muller, J. Appl. Phys. **112**, 114304 (2012).
[25] J. Salfi *et al.*, arXiv:1706.09261 (2017).
[26] A. K. Ramdas and S. Rodriguez, Rep. Prog. Phys. **44**, 1297 (1981).

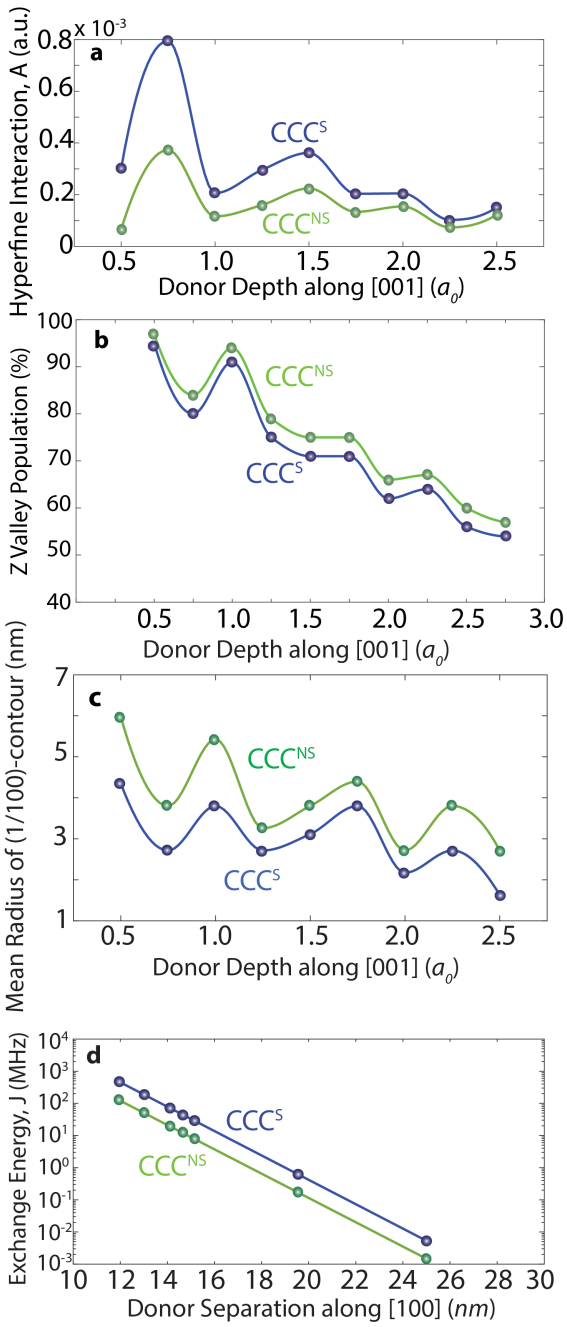

FIG. S1. (a) The peak amplitude of donor wave function charge density ($|\Psi_D|^2$) is plotted as a function of the donor depth below the z=0 surface. The contact hyperfine interaction (A) is directly proportional to the peak of $|\Psi_D|^2$. (b) The relative Z valley population is plotted as a function of the donor depth below the z=0 surface. For a bulk donor ground state, all three valleys equally contribute to the wave function. However the presence of z=0 interface lifts the valley degeneracy and increases the weights of Z valleys. (c) Mean radii of the (1/100)-contours extracted from the charge density of the donor wave functions plotted as a function of donor depth along the [001] direction. (d) Exchange interaction is plotted as a function of P donor separations computed from the two central cell models.

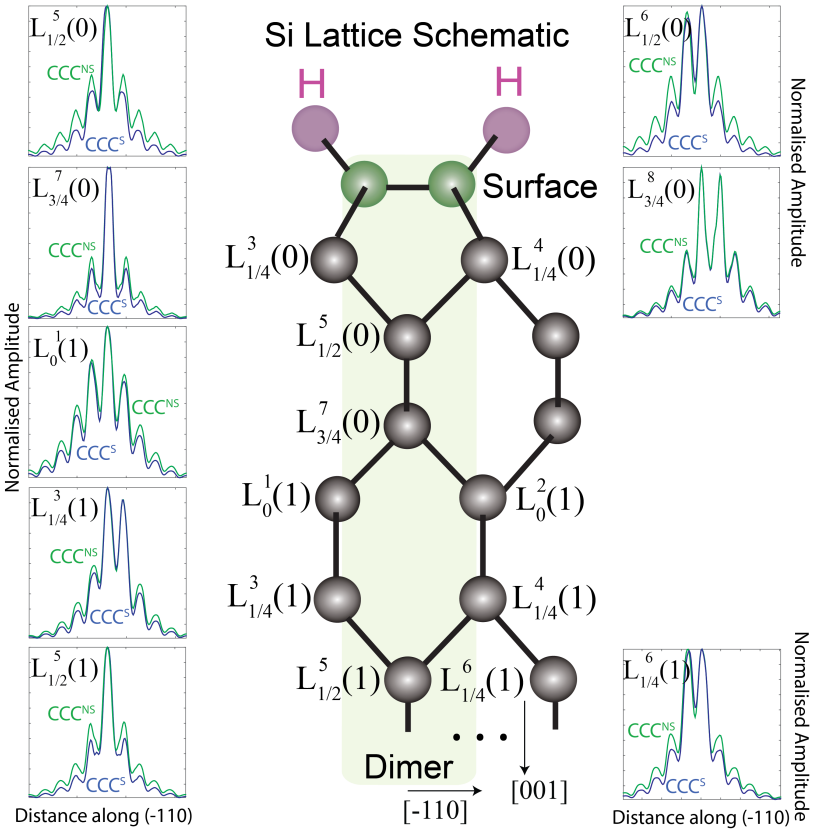

FIG. S2. The calculated real-space STM images are shown in the main text figure 2 for the donor atom positions in the first five unstrained monolayers (ML) below the hydrogen-passivated dimer surface. Here we plot the line cut profiles through the center of images along the (-110) direction, quantitatively highlighting the difference between the STM images computed from the two CCC models.

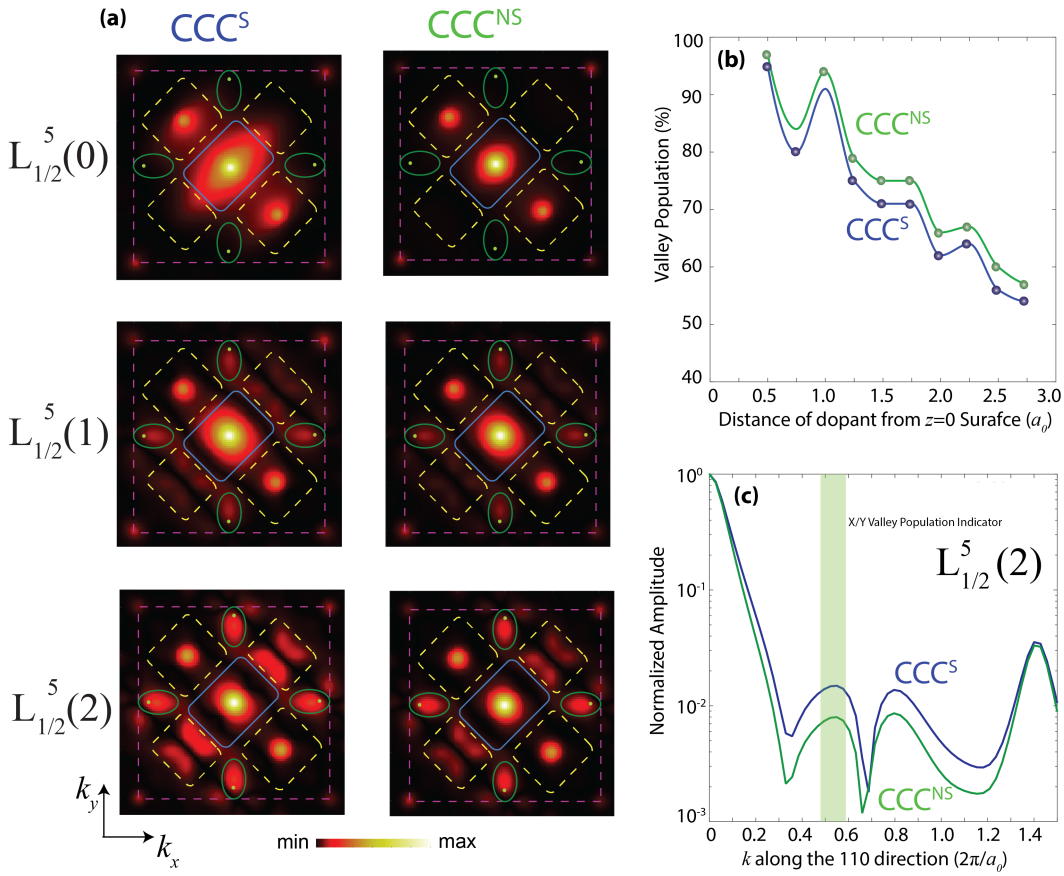

FIG. S3. (a) Fourier transform spectrum of P donor images in $L^5_{1/2}(0)$, $L^5_{1/5}(1)$, and $L^5_{1/2}(2)$ locations computed from the CCC^S and CCC^{NS} models. In each image, the corners of the outer dashed purple box are reciprocal lattice vectors $(2\pi/a_0)$ (p, q), with p=±1 and q=±1. The ellipsoidal structures corresponding to valleys are found within the green ovals and the green dots indicate the position of the conduction band minima: $k_x = 0.85(2\pi/a_0)$ $(\pm 1, 0)$ and $k_y = 0.85(2\pi/a_0)$ $(0, \pm 1)$. The region marked with blue boundary indicates probability envelope and the yellow dashed regions highlight the 2×1 reconstruction-induced features. (b) Z-valley population of the P donor ground states, directly extracted from the Fourier transform of the donor wave function computed from CCC^S and CCC^{NS} models. (c) Line cuts of the Fourier transform spectra of the STM images for P donors in the $L^5_{1/2}(2)$ position, along the k_x=k_y direction. The amplitudes of Fourier transform in the shaded region are directly related to the X=Y valley population of the corresponding donor wave function.

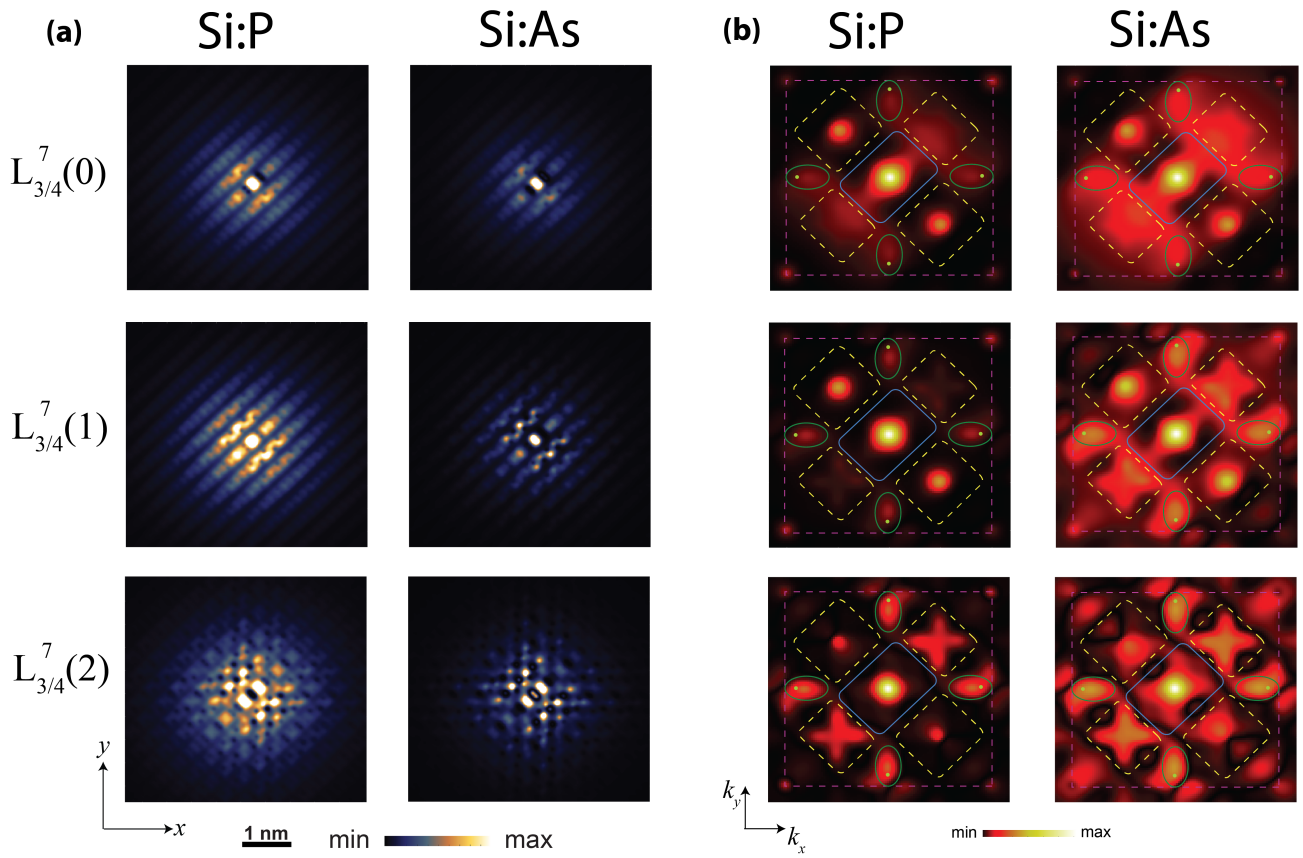

FIG. S4. (a) Real-space images of P and As donors in $L^7_{3/4}(0)$, $L^7_{3/4}(1)$, and $L^7_{3/4}(2)$ locations computed from the CCC^{NS} model. (b) Fourier transform spectrum of P and As donor images in $L^7_{3/4}(0)$, $L^7_{3/4}(1)$, and $L^7_{3/4}(2)$ positions computed from the CCC^{NS} model. In each image, the corners of the outer dashed purple box are reciprocal lattice vectors $(2\pi/a_0)$ (p, q), with p=$\pm$1 and q=$\pm$1. The ellipsoidal structures corresponding to valleys are found within the green ovals and the green dots indicate the position of the conduction band minima: $k_x = 0.85(2\pi/a_0)$ $(\pm 1, 0)$ and $k_y = 0.85(2\pi/a_0)$ $(0, \pm 1)$. The region marked with blue boundary indicates probability envelope and the yellow dashed regions highlight the 2×1 reconstruction-induced features.